Marine Pollution Bulletin 187 (2023) 114610

Contents lists available at ScienceDirect

Marine Pollution Bulletin

journal homepage: www.elsevier.com/locate/marpolbul

Experimental investigation on the nearshore transport of buoyant microplastic particles

Bjarke Eltard Larsen [a,*], Mustafa Ali Abdullah Al-Obaidi [a], Hasan Gokhan Guler [a,b], Stefan Carstensen [a], Koray Deniz Goral [a], Erik Damgaard Christensen [a], Nils B. Kerpen [c], Torsten Schlurmann [c], David R. Fuhrman [a]

[a] Technical University of Denmark, Department of Civil and Mechanical Engineering, DK-2800 Kgs. Lyngby, Denmark
[b] Middle East Technical University, Department of Civil Engineering, Ocean Engineering Research Center, Cankaya, Ankara, Turkey
[c] Ludwig-Franzius-Institute for Hydraulic, Estuarine and Coastal Engineering, Leibniz University Hannover, Hanover, Germany

ARTICLE INFO

Keywords:
Microplastic particles
Buoyant particles
Lagrangian transport velocities
Breaking waves
Non-breaking waves

ABSTRACT

This paper presents experimental measurements of beaching times for buoyant microplastic particles released, both in the pre-breaking region and within the surf zone. The beaching times are used to quantify cross-shore Lagrangian transport velocities of the microplastics. Prior to breaking the particles travel onshore with a velocity close to the Lagrangian fluid particle velocity, regardless of particle characteristics. In the surf zone the Lagrangian velocities of the microplastics increase and become closer to the wave celerity. Furthermore, it is demonstrated that particles having low Dean numbers (dimensionless fall velocity) are transported at higher mean velocities, as they have a larger tendency to be at the free-surface relative to particles with higher Dean numbers. An empirical relation is formulated for predicting the cross-shore Lagrangian transport velocities of buoyant microplastic particles, valid for both non-breaking and breaking irregular waves. The expression matches the present experiments well, in addition to two prior studies.

1. Introduction

In the order of millions of tons of plastic enter the world's oceans every year (Zhang, 2017; Kooi et al., 2017; van Sebille et al., 2020). Jambeck et al. (2015) estimated that the cumulative amount of plastic waste entering the ocean may increase by an order of magnitude by 2025, relative to 2010. Plastic waste has been observed in nearly all marine environments, even in those with minimal human presence, such as polar regions and beneath ice caps (Barnes et al., 2009; Browne et al., 2011; Cozar et al., 2014; Nerland et al., 2014; van Sebille et al., 2015; Zhang, 2017; Lamb et al., 2018; Wieczorek et al., 2018; van Sebille et al., 2020).

One category of plastic waste of growing concern is microplastic particles (less than 5 mm in size), which can stem from either primary (originally small particles e.g. used in consumer products, Zhang, 2017; Kooi et al., 2017) or secondary sources (small fragments of larger pieces of plastic). Microplastics can have a variety of shapes e.g. spheres, fibers, cylindrical beads, or irregular shapes (Zhang, 2017), and can likewise have a wide range of densities, meaning that they can be either buoyant or non-buoyant.

In the ocean the Stokes drift (the average velocity of a fluid particle, which is in the direction of wave propagation near the free surface) can be expected to be important for buoyant plastic particles. However, whether fluid and foreign particles actually travel with the theoretically predicted drift velocity of the fluid remains an open question (van Sebille et al., 2020). For instance, Deike et al. (2017) studied deep-water focused wave groups using computational fluid dynamics (CFD) and found that particle velocities were well predicted using the deep-water Stokes drift velocity for non-breaking waves. For breaking focused wave groups, they found that particle velocities increased relative to Stokes drift velocity. The particle transport velocities were likewise very dependent on their position relative to the breaking point. Particles located just onshore of the overturning wave were observed to travel faster than those located both offshore, and further onshore, of the break point. This finding was confirmed experimentally by Lenain et al. (2019) using buoyant plastic particles. Pizzo (2017) utilized the same model as Deike et al. (2017) and derived a criterion for when particles "surf" on the breaking wave, making them travel approximately at the wave

* Corresponding author.
E-mail address: bjelt@mek.dtu.dk (B.E. Larsen).

https://doi.org/10.1016/j.marpolbul.2023.114610
Received 3 November 2022; Received in revised form 3 January 2023; Accepted 9 January 2023
Available online 18 January 2023

celerity. Recently, Calvert et al. (2021) described analytically how relatively large particles can be expected to travel at velocities above those predicted by the Stokes drift in non-breaking deep-water waves.

In the above studies the particles were either considered as passive tracers (Deike et al., 2017; Pizzo, 2017) or were larger than the microplastic regime (Lenain et al., 2019; Calvert et al., 2021). Furthermore, the studies focused on deep-water waves, whereas there have been relatively few studies focusing on the transport mechanisms of buoyant microplastic particles in nearshore coastal regions (van Sebille et al., 2020). Alsina et al. (2020) utilized video cameras and tracked the paths of buoyant and non-buoyant microplastic particles (including both micro- and larger plastics) in a small scale laboratory facility, under intermediate-depth non-breaking monochromatic waves. They investigated the influence of the wave period, plastic size and density, and expectedly found that buoyant particles travel with a speed close to that of the wave-induced Lagrangian fluid particle velocity. Forsberg et al. (2020) investigated the cross-shore transport of buoyant and non-buoyant microplastic particles in a small-scale wave flume, utilizing monochromatic waves and a plane rigid sloping bed. They likewise investigated the effect of wind on these transport patterns. Without wind, the non-buoyant particles had a tendency to accumulate around the break point, whereas the buoyant particles primarily accumulated at the beach. In the case of an offshore-directed wind the buoyant particles tended to be transported offshore, whereas the wind had little effect on the non-buoyant particles. Kerpen et al. (2020) carried out physical model experiments on a live sediment bed with different buoyant and non-buoyant irregularly-shaped microplastic particles under monochromatic breaking waves, investigating the wave-induced distribution of the microplastic particles. For the non-buoyant particles, the accumulation was seen to depend on a dimensionless fall velocity. Finally, Guler et al. (2022) studied the transport patterns of non-buoyant particles in a small-scale wave flume under irregular breaking and non-breaking waves. They identified four different accumulation hotspots along the coastal profile and the non-dimensional Dean number as an important factor in determining these.

With the exception of Guler et al. (2022), the previous studies have all utilized monochromatic waves, and the Lagrangian velocities of the particles have only been investigated in non-breaking waves (Alsina et al., 2020). The present study aims to further improve the quantitative understanding of wave-induced cross-shore transport of buoyant microplastic particles beneath both non-breaking and breaking irregular waves. This will be done by performing detailed experiments in a state-of-the art coastal engineering wave flume. In the experiments to be described, particles having different shapes and densities were released at different locations and their beaching time recorded. Based on the statistical differences in beaching times from different drop locations, the Lagrangian transport velocities will be estimated. The present study will extend previous research on the transport of buoyant microplastic particles by utilizing (more realistic) irregular waves, and also by quantifying the Lagrangian particle transport velocities both outside and within the surf zone.

The remainder of the present paper is structured as follows: The experimental setup and procedure is described in Section 2. Results are presented and analyzed in Section 3, and a novel expression for the Lagrangian microplastic particle transport velocities is developed and further validated in Section 4. Results are discussed in Section 5. Finally, conclusions are drawn in Section 6.

2. Experimental setup and procedure

2.1. Microplastic particles

The present experiments used three different microplastic particle groups. Photographs representing each group can be seen in Fig. 1. Material, densities (ρ_p), dimensions, mean rise velocity w_r and standard deviation of the rise velocity σ_r of each of the particle groups are given in Table 1.

Particle 1 corresponds to spherical EPS (expanded polystyrene) particles, acquired from a local Panduro Hobby store. The particles are sphere-like (many also resembling ellipsoids) with length scales typically ranging between 4 and 6 mm (we will refer to these as spheres for simplicity). Particle 2 corresponds to closed hollow ABS (acrylonitrile butadiene styrene) cubes, which were 3D printed using an ANYCUBIC 4MAX Pro 2.0 printer, with a printing precision of approximately ±0.1 mm. Particle 3 corresponds to PE (polyethylene) open hollow cylinders with a wall thickness of 1 mm (these are actually Hama beads for pegboards).

The particle densities were found by simultaneously weighing 50 particles of each type and dividing by their combined volume (for the EPS spheres a spherical shape and a diameter of 5 mm was assumed). The rise velocity was measured in a filled, but otherwise empty, flume in the Hydraulics Laboratory at the Technical University of Denmark (DTU). Inside the flume (approximately 30 cm from the side wall) two vertical rulers were mounted on either side of the rising particles. The particles were released approximately 4 cm from the bottom through a hollow tube positioned at an angle, to not disturb the rising particles. The particles were pushed through the tube with a thin rod. Great care was taken to ensure that air bubbles did not stick to the particles when releasing them. The rising of the particles was recorded with a Nikon D5600 camera, focusing on the region from 20 cm to 45 cm above the flume bottom. Twenty randomly selected particles from each particle group were tested with statistical quantities (w_r and σ_r based on results using these samples). For Particle 2 (hollow cubes), one out of 20 particles travelled significantly slower than the others. From the video analysis of this case very small bubbles were visible on the outside, believed to be air bubbles leaking from within the cube. This made the particle heavier thus explaining the slower rise velocity. The mean value reported in Table 1 includes this particle (as this particle was sampled from those used in experiments). The mean value neglecting this particle was only 1.5 % higher, indicating that is of little importance for the end results.

2.2. Experimental setup

The present experiments, concerning the nearshore transport of buoyant microplastic particles, were conducted in a 28 m long, 0.8 m deep and 0.6 m wide wave flume at DTU, equipped with a piston-type wavemaker with active wave absorption. Fig. 2 shows a sketch of the

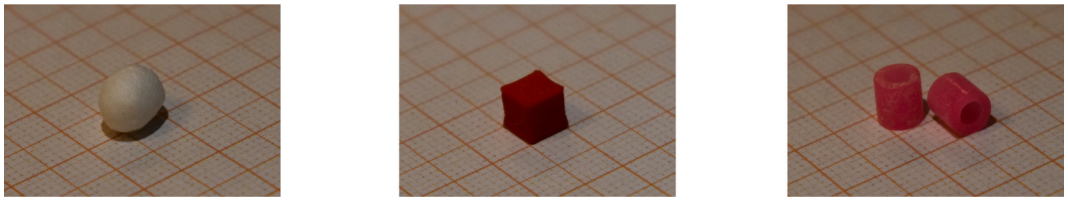

(a) Particle 1: An EPS sphere (b) Particle 2: A hollow ABS cube (c) Particle 3: Hollow PE cylinders

Fig. 1. Representatives for the three microplastic particle groups used in the experiments lying on millimetric paper.

Table 1
Properties and dimensions of the three particle types utilized in the experiments. The Dean number Ω_r (defined in Eq. (10)) corresponding to the present experimental conditions is also provided in the last column.

No.	Shape	Material	Length (mm)	Height (mm)	Width (mm)	ρ_p (kg/m^3)	w_r (m/s)	σ_r (m/s)	Ω_r
1	Spheres	EPS	4–6	4–6	4–6	55	0.254	0.012	0.41
2	Hollow cubes	ABS	5	5	5	665	0.129	0.011	0.80
3	Hollow cylinders	PE	5	5	5	907	0.053	0.001	1.95

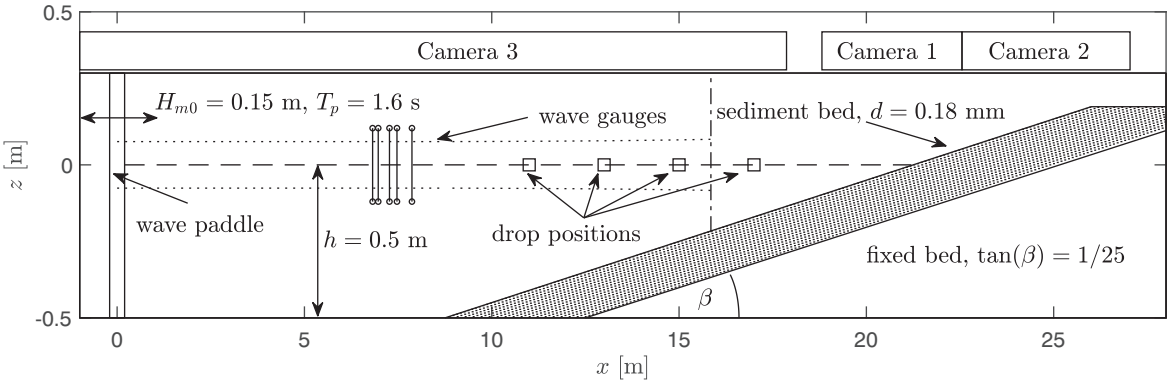

Fig. 2. Sketch of the experimental wave flume setup. Included are also the predicted surface elevation maxima and minima using linear theory (dotted lines) and an incipient breaking criterion of $H_{m0}/h = 0.77$ (vertical dot-dashed line).

setup, including positions of the wave gauges, the approximate field of view for Cameras 1–3, used for video recordings, and the drop positions for the microplastic particles (all of which will be discussed in more detail in what follows). The origin of the coordinate system is placed at the still water level at the wave paddle, with the horizontal x axis pointing onshore and the vertical z axis upward.

Beginning at $x = 12.5$ m a constant fixed slope $\tan(\beta) = 1/25$ was installed, and a 15 cm layer of well-sorted sand with median grain diameter $d = 0.18$ mm was added on top of the slope. A sediment beach slope was utilized rather than a rigid bed, as a sediment bed can influence the run-up of the waves as well as the depositional behavior of the microplastic particles, which we expect could beach more easily on sand relatively to a smooth bed. Throughout the experiments the water depth offshore of the sloping region was kept constant at $h = 0.5$ m. Offshore of the slope five resistance type wave gauges were installed to measure the surface elevations and determine the wave heights and other statistics for the incoming waves. The incoming wave signal, which repeated itself every 30 min, corresponds to irregular waves based on the JONSWAP

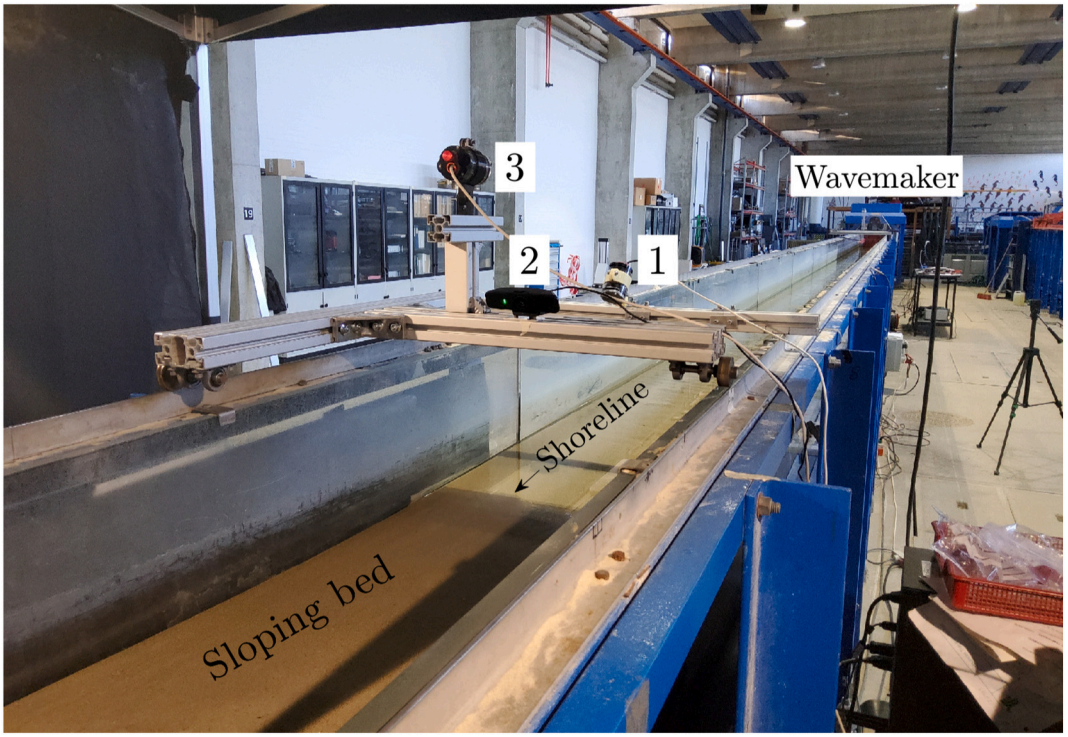

Fig. 3. Photograph depicting wave flume and camera setup (Cameras 1–3) used to record particle drop and beaching times.

spectrum, using a peak enhancement factor $\gamma = 3.3$. The generated waves had a peak period $T_p = 1.6$ s and a measured spectral significant wave height near the toe of the slope

$$H_{m0} = 4\sigma_\eta = 0.15\,\text{m} \quad (1)$$

where σ_η is the standard deviation of the measured surface elevations, η. The generated waves were intermediately-deep with $k_p h = 1$, where k_p is the peak wave number, with characteristic steepness $k_p H_{m0} = 0.3$. In the present experiments measurements of the surface elevation could not be performed above the sloping bed due to the placement of the cameras, which were used to record the particle transport. However, the utilized wave climate and initial slope are identical to the initial part of the reference case reported in a study on beach nourishment (without microplastic particles) of Larsen et al. (2023). In these experiments surface elevations were also measured on the slope of the profile, and therefore surface elevations measurements from these experiments will likewise be presented to complement the analysis.

The experiments were recorded using five digital cameras. Three (Cameras 1–3) were mounted near the shoreline on a trolley above the flume as can be seen in Fig. 3. Additionally, two (Cameras 4 and 5) were mounted at the side of the wave flume looking through the glass walls. For the three cameras mounted near the shoreline, Camera 1 and 2 were used to record the waves and microplastic particles as they arrived at the shore, whereas Camera 3 was used to record when the particles were dropped into the flume. Cameras 4 and 5 were mounted at $x = 12$ m and $x = 18$ m, respectively, to be able to view and record how the particles behaved before, during and after wave breaking. Cameras 4 and 5 were additionally used to quantify the fraction of waves breaking within their field of view.

A single downward-looking Omron ZX1-LD600 laser distance meter, mounted on a trolley on the top of the flume, was used to track the vertical position of the bed. The position of the trolley was measured by a horizontal-looking SICK DT50–2 laser distance meter mounted at the beach end of the flume. The vertical laser distance meter had an accuracy of ±0.5 mm, and the horizontal laser distance meter an accuracy of ±5 mm. The laser distance meter was used to record the bed profile before and after a series of waves.

2.3. Procedure and data treatment

We will now present the experimental procedure as well as the treatment of the gathered data. The wave paddle was turned on and the waves were allowed to propagate for 30 s before the first controlled drop of particles occurred. Release of particles occurred at four different cross-shore positions: $x = 11$ m, $x = 13$ m, $x = 15$ m and $x = 17$ m, see Fig. 2. The cross-shore positions were chosen such that particles were released both far from breaking, around incipient breaking and well inside the surf zone. At each position 50–75 particles from one of the particle groups were released simultaneously. These particles were allowed to beach (a process that took O(5 min)), and during this time beached particles were manually removed. When all the particles had beached, the collected particles were re-released at the same cross-shore location. This process continued for 1 h. To release the particles a plastic cup was used. For the first drop in an experimental series, the cup contained only dry particles. After the particles had beached the first time, they were manually picked up and inserted into the cup, along with a small amount of water to prevent the now-wet particles from sticking to the sides of the container. For Particle 2 (hollow cubes) and Particle 3 (hollow cylinders), the cup contained 50 particles for the first drop, whereas it contained 75 particles for Particle 1 (spheres). The additional number of particles for Particle 1 were used, due to their greater tendency to stick to the cup side. To allow for a quick (nearly simultaneous) drop, any particles sticking to the cup were not dropped into the flume. Therefore, to ensure a similar number of particles being released as for the two other groups, 75 particles were used for Particle 1. After 1 h, the particles were then released at the next cross-shore position and the process was repeated for the same duration. The repeated release of particles at the same location was done to ensure that the particles experienced all parts of the irregular wave signal and to obtain stable statistics.

The 1 h duration was determined based on initial tests with Particle 3, where the experiments were conducted for 1.5 h. Fig. 4a,b shows a comparison of the probability density functions (PDFs), where p is probability density, for the beaching time (t_b) from two different cross-shore drop locations plotted after 1 and 1.5 h respectively. Fig. 4c, d additionally shows the development in the mean ($\overline{t_b}$) and standard deviation (σ_b) of the beaching times with the number of particles used in these two drop positions. As can be seen there are only minor differences between the PDFs having different durations (difference between black and red lines in Fig. 4a,b), and it can also be seen that both mean and standard deviation of t_b stabilized after approximately 400 particles. Running the experiments for 1 h before changing cross-shore location resulted in a minimum of 491 particles of any type released in each position. It is therefore safe to assume that the mean and standard deviation of the beaching times have converged for the given wave spectrum and beach profile.

Each wave series was conducted for a total of 2 h (corresponding to two different drop locations for one particle group per wave series). After this, the experiments were stopped and the profile was manually reshaped to a 1/25 slope, before continuing the experiments, following same procedure as described above. The limited duration of the experiments was chosen due to the live sediment bed which would evolve over long durations. The limited duration ensured that all drops of particles had very similar (if not identical) bathymetric conditions. That the bed did not change significantly during the 2 h duration can be seen from Fig. 5a, which shows the initial bed profile and the bed profile after 2 h of experiments. Fig. 5b shows the erosion/deposition of the seabed over this duration. The absolute change in bed level $|\Delta z_b|$ at any cross-shore position was generally less than 0.02 m and it can therefore be expected that the wave climate will not be significantly affected by the morphological change. This contention is also supported by the measurements of surface elevations from Larsen et al. (2023) (not shown here for brevity), where measured wave statistics were almost identical, even over 5 h durations.

A particle was considered beached when it was (1) stationary onshore of the still water level and (2) water had receded during draw down. The latter condition means that a particle deposited onshore is not considered beached until the water had withdrawn fully. At the time of full draw down the number of deposited particles recorded by Camera 1 and 2 were counted. During the experiments beached particles were manually removed using tweezers, to ease counting of additional particles in the videos. The total number of stationary particles visible in Camera 1 and 2, along with the number of particles already removed from the flume, constitute the number of beached particles at any given time. Occasionally, an already-beached particle was not collected quickly enough and was taken offshore by a subsequent wave. In such cases the particle retained its original beaching time, and was assumed to correspond to the next beached particle to ease accounting (to also avoid attributing two beaching times to the same particle).

In addition to recording the particle movement at $x \approx 12$ m and $x \approx 18$ m, Cameras 4 and 5 were also used to quantify the fraction of waves breaking, Q, at these cross-shore locations (this will be shown in the forthcoming Fig. 6). To determine Q, the number of waves breaking during a 10 min span at three different locations within each camera's frame of view have been counted, which were then divided by the approximate number of waves passing over the same duration. The number of waves passing during the 10 min duration has been estimated by dividing the duration by the mean zero crossing period of the incoming waves, $T_z = 1.35$ s.

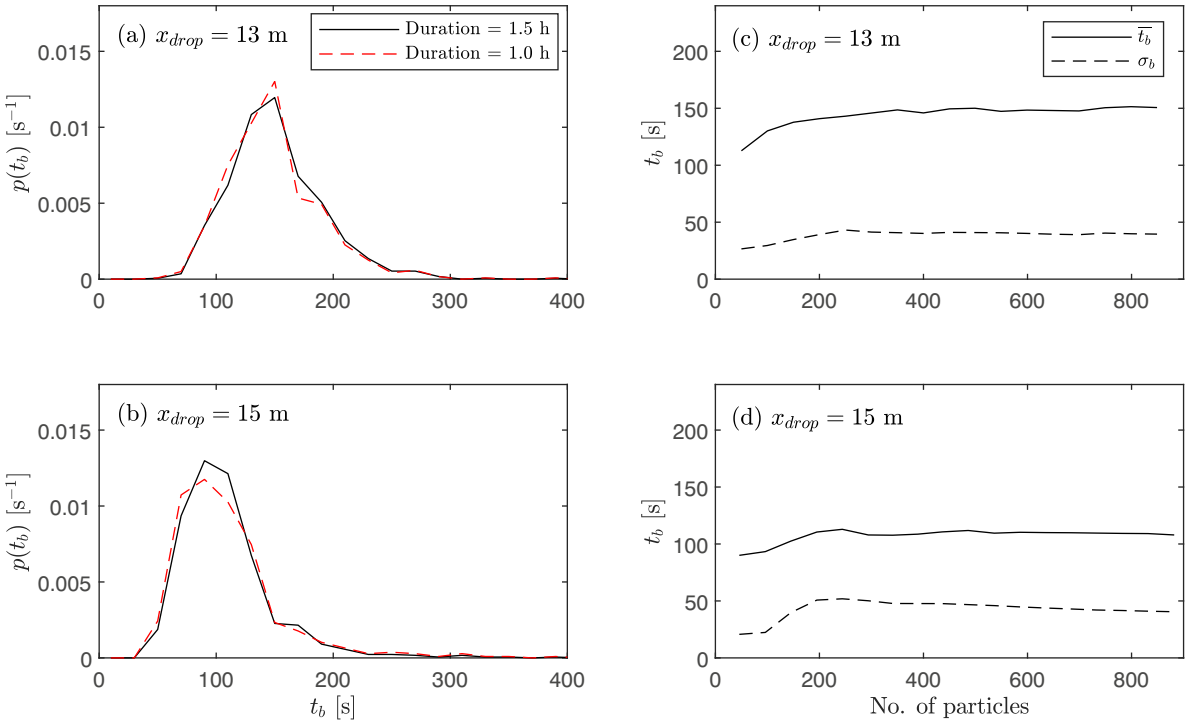

Fig. 4. PDFs for Particle 3 (hollow cylinder) beaching times t_b after 1.0 h and 1.5 h durations, released at (a) $x = 13$ m and (b) $x = 15$ m. Convergence in mean and standard deviation of t_b with number of particles dropped at (c) $x = 13$ m and (d) $x = 15$ m.

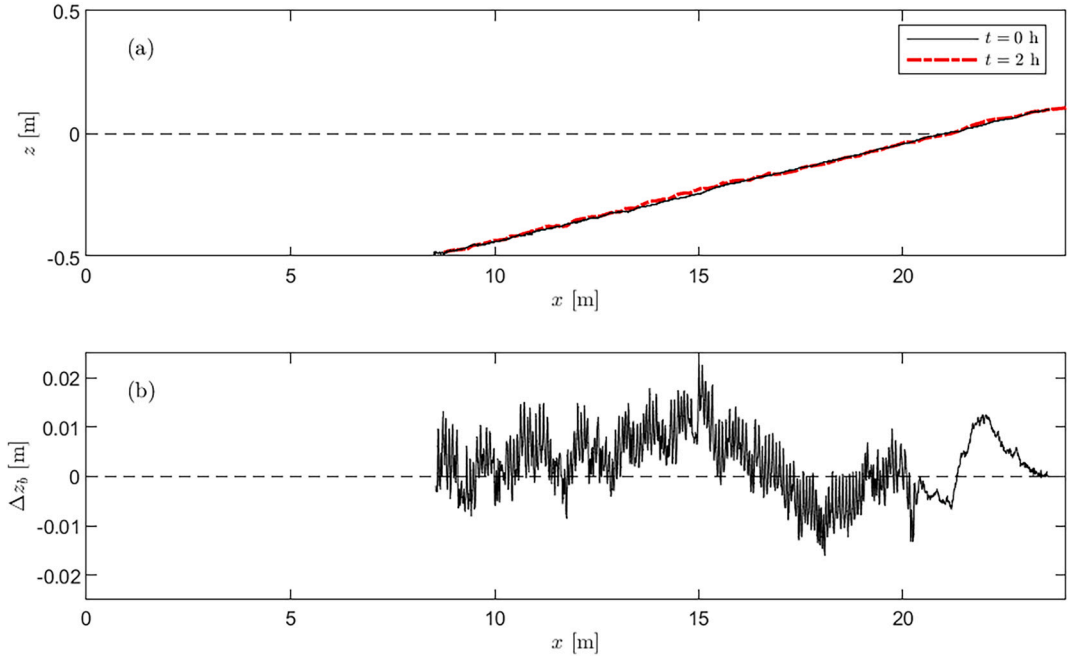

Fig. 5. (a) Measured bed elevations z_b and (b) change after 2 h. Δz_b.

3. Results

We will now present and analyze results from the experiments described above. First, the measured wave characteristics will be presented, to provide an overview of the climate in the flume. These will be followed by a presentation of beaching times and finally cross-shore microplastic particle transport velocities.

3.1. Wave characteristics

In this subsection we will present statistics of the wave climate based on surface elevation measurements from Larsen et al. (2023) again using the same generated waves and bottom bathymetry, accompanied with the measurements of Q from the present experiments. Fig. 6 shows the initial bed profile (Fig. 6a), spectral significant wave height H_{m0} (Fig. 6b), surface elevation skewness.

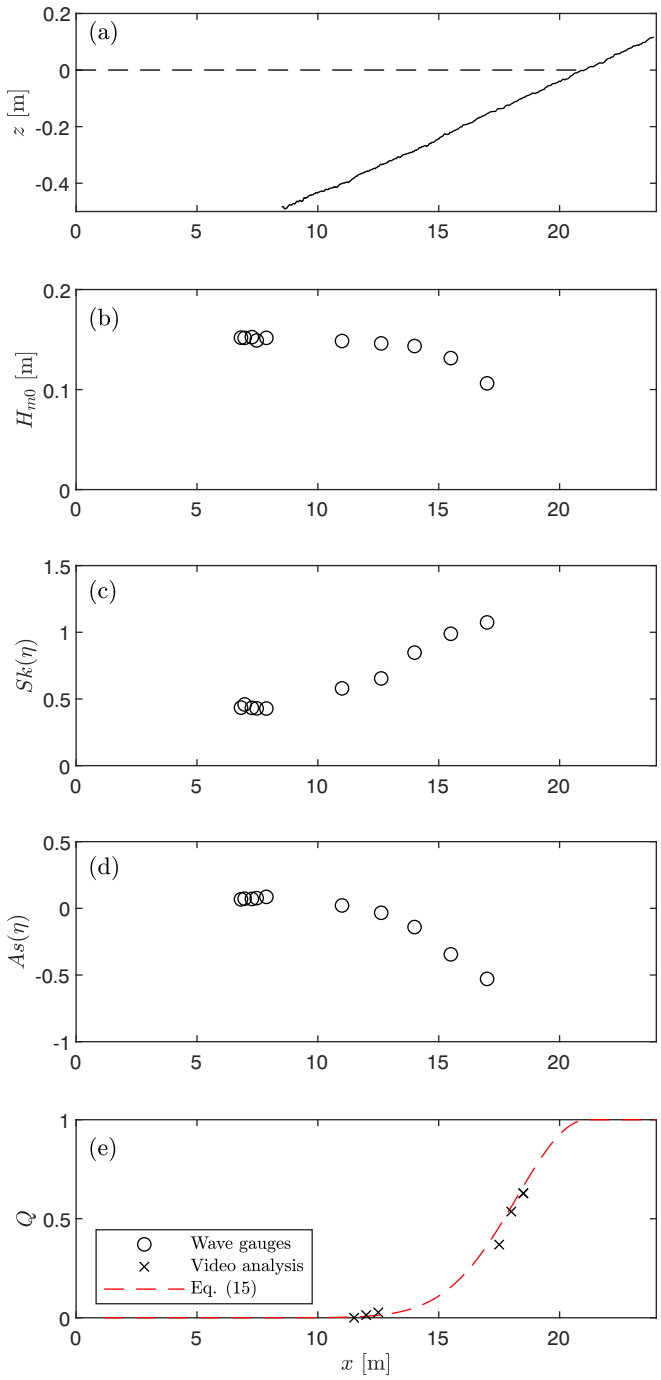

Fig. 6. Measured (a) bed elevations, (b) spectral significant wave heights, (c) skewness, (d) asymmetry and (e) fraction of breaking waves. Wave gauge data corresponds to the initial measurements from the reference case of Larsen et al. (2023), using the same wave conditions and bathymetry as in the present experiments.

$$Sk(\eta) = \frac{\langle \eta^3 \rangle}{\sigma_\eta^3} \tag{2}$$

(Fig. 6c), surface elevation asymmetry

$$As(\eta) = \frac{\langle \mathscr{H}(\eta)^3 \rangle}{\sigma_\eta^3} \tag{3}$$

(Fig. 6d) and fraction of breaking waves Q (Fig. 6e). In the above, the angular brackets represent time-averaging and $\mathscr{H}$ is the Hilbert transform. The skewness characterizes the degree of asymmetric variation of the surface during crest and trough regions, whereas the asymmetry characterizes the degree of front-back asymmetry in the waves. Note that negative *As* corresponds to forward-leaning waves. Fig. 6b shows that the spectral significant wave heights are nearly constant for the initial part of the sloping profile, until $x \approx 15$ m where the wave height starts to decay significantly. This indicates some degree of wave breaking, which is supported by the skewness increasing and the asymmetry decreasing (Fig. 6c,d) along the beach slope, reaching levels typical of the surf zone in the literature (see e.g. Brinkkemper et al., 2016; Larsen et al., 2020). This description is also consistent with the measured fraction of breaking waves Q (Fig. 6e) which increases from a few percent at $x \approx 12$ m to more than 50 % at $x \approx 18$ m. For the present beaching time experiments, this means that the most offshore drop position, $x_{drop} = 11$ m, will have experienced a negligible number of breaking waves, whereas the most onshore drop position, $x_{drop} = 17$ m, experienced close to 50 % of the waves breaking. (Included in Fig. 6e as the dashed line is also the fraction of waves breaking, as predicted by forthcoming Eq. (15), which will be discussed in more detail in Section 4.)

From both video analysis and visual observation it was found that the waves predominantly broke as spilling breakers, though occasional plunging breakers were also observed. Plunging breakers are characterized by a complete overturning of the wave crest which then plunges into the wave trough in front, whereas spilling breakers are characterized by an unstable wave crest which gradually spills down the front of the wave creating a large air-water mixture. The surf similarity parameter of the present experiment is

$$\xi_\infty = \frac{tan\beta}{\sqrt{H_{m0,\infty}, L_{p,\infty}}} = 0.2 \tag{4}$$

where $L_{p,\infty} = 2\pi/(gT_p^2)$ is the deep-water peak wave length and $H_{m0,\infty}$ is the deep-water wave height, which has been estimated using linear wave theory, assuming conservation of energy flux:

$$H_{m0,\infty}^2 = H_{m0}^2 \left(1 + \frac{2k_p h}{sinh(2k_p h)}\right) tanh(k_p h) \tag{5}$$

Therefore the observation of breaker type is consistent with the classification from Galvin (1968), which indicates that $\xi_\infty < 0.5$ will result in spilling breakers. See also Chapter 7 of Sumer and Fuhrman (2020).

3.2. Beaching times and Lagrangian transport velocities

We will now present results for the measured beaching times as well as derived Lagrangian microplastic particle transport velocities. Fig. 7 shows PDFs and cumulative distributions functions (CDFs, where P is the cumulative probability) for the beaching times t_b, for all particle groups at all four release locations. For all three particle groups the beaching times naturally decrease as the drop position moves closer to the shoreline (i.e. the PDFs and CDFs are further left in Fig. 7), as expected. This trend can likewise be seen from the mean values in Table 2, which summarizes the main statistics for the beaching times i.e. mean (indicated by overbar), standard deviation σ_b and skewness. Table 2 likewise shows that the standard deviation of the beaching times generally decrease as the drop location moves closer to the shoreline, and that the beaching times are mostly positively skewed (indicating that the PDFs are leftward leaning in Fig. 7a,c,e). In all three cases the distance between the CDF for $x_{drop} = 15$ m and $x_{drop} = 17$ m are closer together than those for $x_{drop} = 11$ m and $x_{drop} = 13$ m, as well as for $x_{drop} = 13$ m and $x_{drop} = 15$ m. This indicates a markedly faster cross-shore Lagrangian transport velocity for the particles in this region of the flume, which is also expected due to the increased number of breaking waves.

In Fig. 8 the beaching times from Fig. 7 are recast, now organized by drop position, allowing for more direct comparison of beaching times

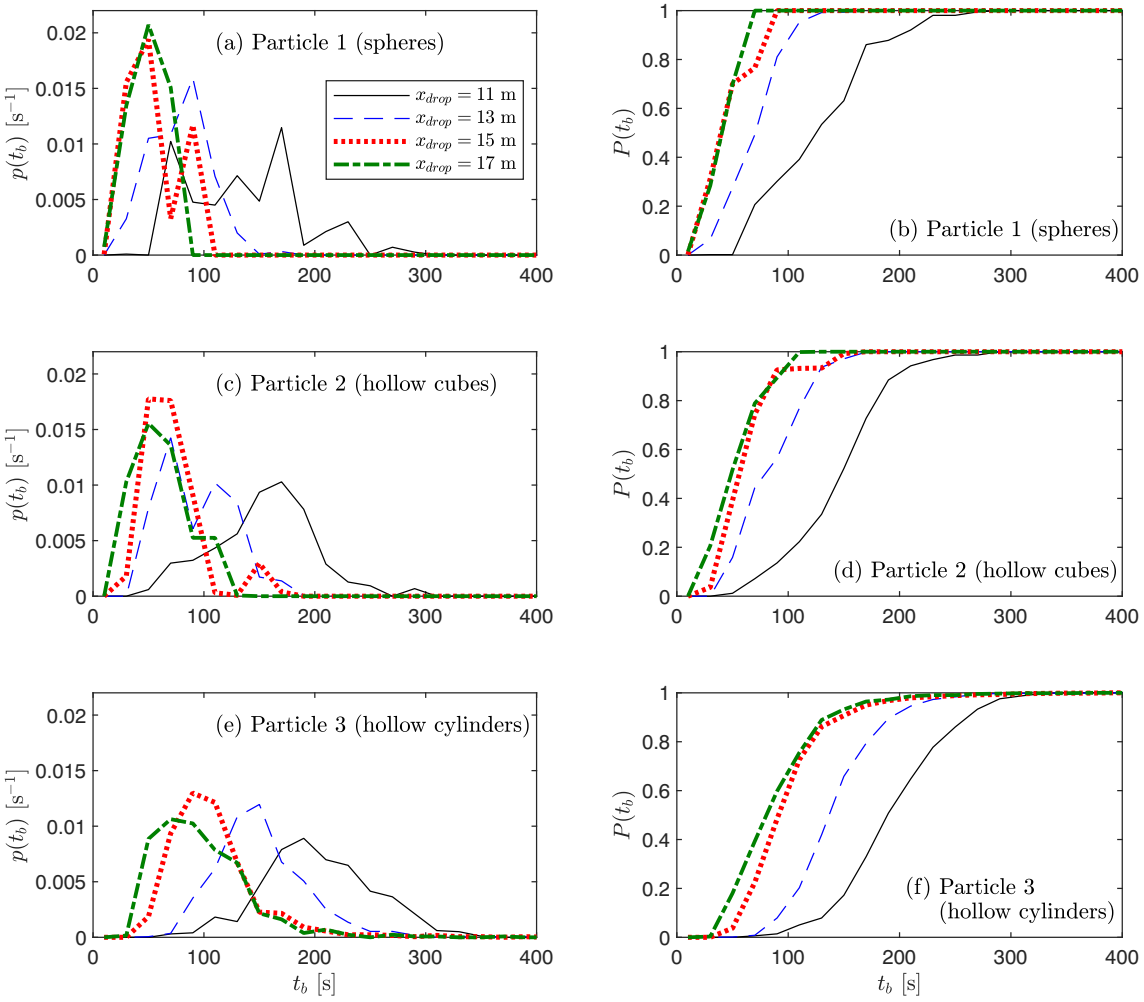

Fig. 7. PDFs (left) and CDFs (right) for the beaching time t_b for particles released various different drop positions.

Table 2
Beaching time statistics for the three particle groups released from the four different drop positions.

Particle	x_{drop} [m]	$\bar{t}_b$ [s]	σ_b [s]	$Sk(t_b)$
1	11	136.6	48.9	0.57
1	13	78.6	26.1	0.42
1	15	52.6	21.5	0.46
1	17	47.2	15.0	−0.49
2	11	154.0	43.9	0.10
2	13	91.4	31.2	0.46
2	15	70.6	25.7	1.42
2	17	60.9	22.8	0.55
3	11	202.4	48.2	0.15
3	13	150.6	39.5	0.97
3	15	107.9	40.5	2.07
3	17	95.3	41.8	1.76

between the three particle groups. From Fig. 8 it is clear that for all four drop locations Particle 1 had the lowest beaching times (CDFs most leftward) and Particle 3 had the highest beaching times (CDFs most rightward). As Particle 1 ($w_r = 0.254$ m/s) had the largest rise velocity and Particle 3 ($w_r = 0.053$ m/s) the lowest, this indicates clear dependence of the beaching times, and thus Lagrangian particle transport velocities u_p, on the rise velocity of the particles.

We will now focus on the Lagrangian velocities of the particles, u_p. These have been estimated from

$$u_p = \frac{\Delta x_{drop}}{\Delta \bar{t}_b} \tag{6}$$

where Δx_{drop} is the distance between adjacent drop positions, and $\Delta \bar{t}_b$ is the difference in mean beaching times observed between these positions. Fig. 9 shows the cross-shore evolution in Lagrangian microplastic particle transport velocities, u_p, where the x locations have been calculated as the average between two drop positions. Included in Fig. 9, as reference lines, are also the variation of the linear shallow-water wave celerity $\sqrt{gh}$, as well as the deep-water wave-induced Lagrangian fluid particle velocity

$$U_\infty = \left(\frac{H_{m0,\infty}}{2}\right)^2 \omega_p k_{p,\infty} \tag{7}$$

where $\omega_p = 2\pi/T_p$ is the peak angular frequency and $k_{p,\infty} = 2\pi/L_{p,\infty}$ is the peak deep-water wave number. At $x = 12$ m, u_p is small and the three particle groups travel at almost the same velocity. The Lagrangian particle transport velocities are close to U_∞, which could be expected as very few waves broke in this part of the flume. At $x = 14$ m, u_p of Particle 3 is still very close to U_∞, but that of Particle 1 and Particle 2 have approximately doubled. At $x = 16$ m all three particles have u_p significantly larger than U_∞, becoming within an order of magnitude of $\sqrt{gh}$. At $x = 16$ m, u_p for the three different particle groups clearly depends on the rise velocity, with Particle 1, again having largest rise velocity, being transported fastest, as previously eluded to.

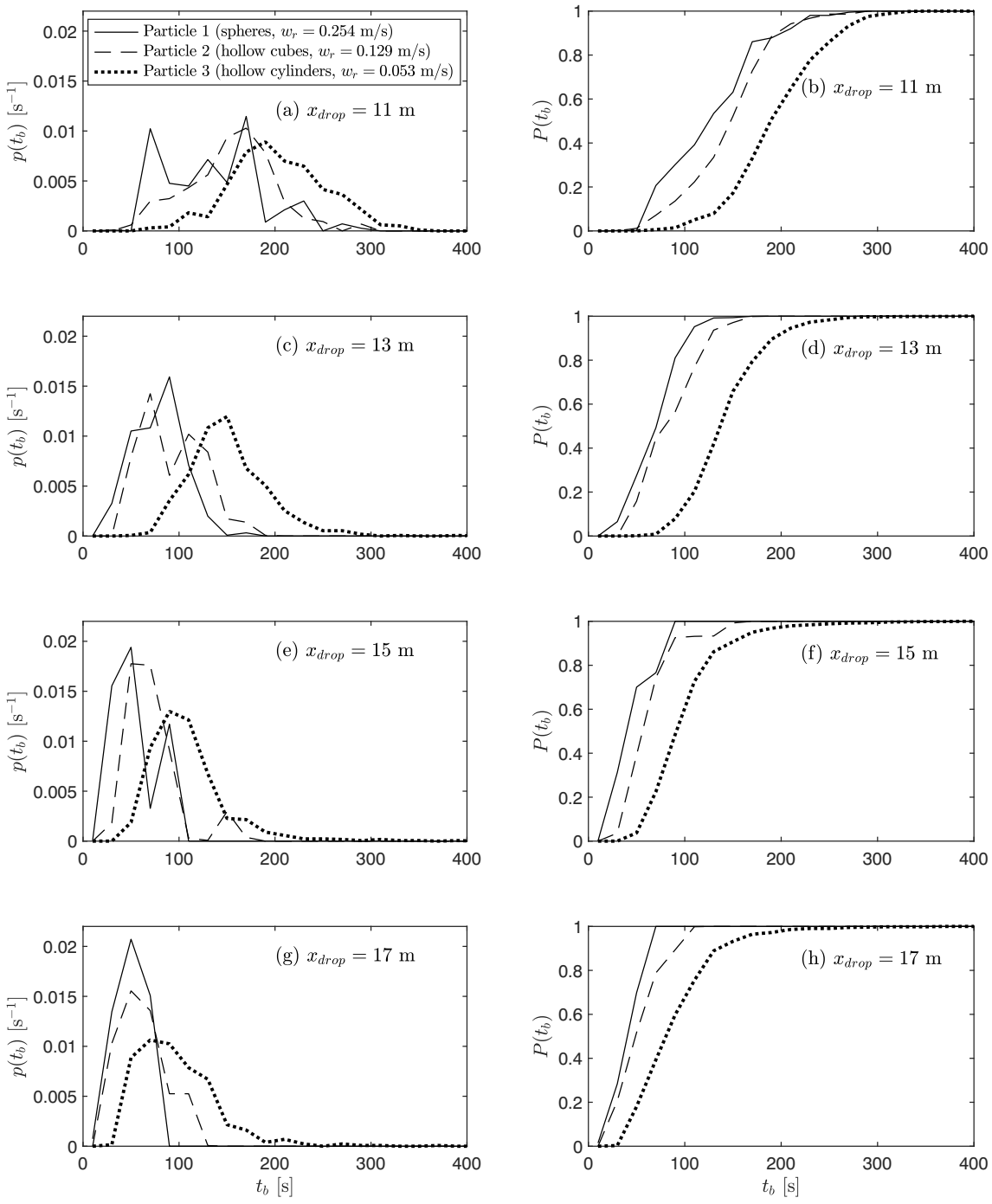

Fig. 8. Probability density(left) and cumulative probability (right) function for all three particle groups released at (a) $x_{drop} = 11$ m, (b) $x_{drop} = 13$ m, (c) $x_{drop} = 15$ m and (d) $x_{drop} = 17$ m. Note that the data shown here is same as in Fig. 7, just organized differently.

The picture presented in Fig. 9 is consistent with our prior expectations and understanding of the transport processes, which we have sketched in Fig. 10, and we will now further discuss. Prior to breaking, the particles can be expected to move with a velocity near the wave-induced Lagrangian fluid particle velocity (see e.g. Alsina et al., 2020; Calvert et al., 2021), here approximated as Eq. (7). The rise velocity is not important as all buoyant particles essentially remain on the surface at all times. In the surf zone, however, the particles are often captured by ("surfing" on) the breaking waves, and can therefore be expected to travel with a speed closer to the wave celerity. The particles do not typically remain within the breaking wave front indefinitely, however. After some time/distance they rather become submerged, falling beneath the wave front and becoming left behind. This is consistent with numerical simulations and experiments of particle transport in deep-water breaking waves (Deike et al., 2017; Lenain et al., 2019). In situations with large rise velocity, there is a lower probability of falling beneath the breaking wave front, as the rise velocity can counteract downward velocities inside the swirling breaking bore front. Simultaneously, a larger rise velocity also means that there is greater likelihood of being captured by a subsequent breaker, as the particle will more quickly return to the free-surface after being submerged. This scenario is illustrated in Figs. 11 and 12, showing snapshots from Camera 5 at $x \approx 18$ m. In Fig. 11 three particles (inside the red circles; Particle 1, spheres, $w_r = 0.254$ m/s), have been submerged beneath the wave front, but have

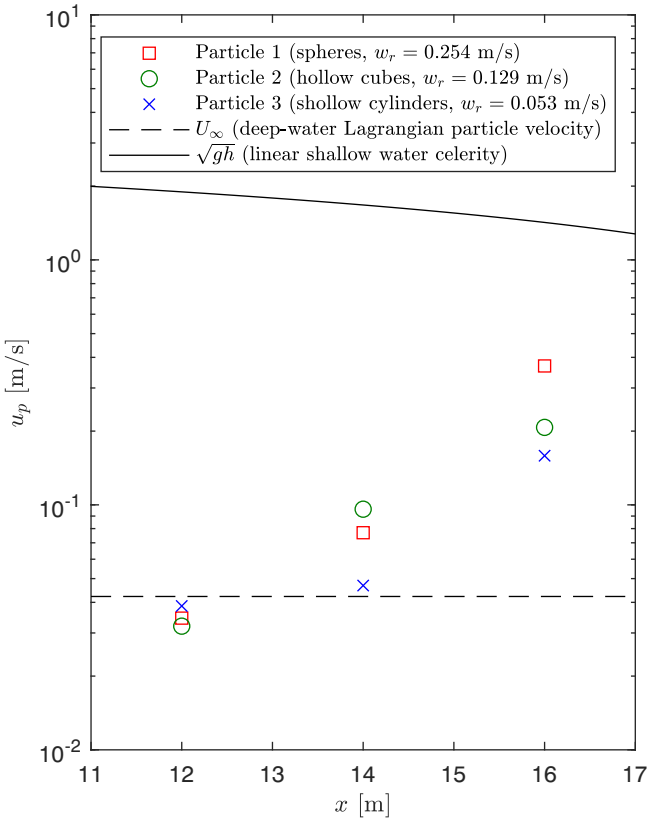

Fig. 9. Cross-shore development of the Lagrangian microplastic particle transport velocities u_p.

risen to the free surface almost immediately. In Fig. 12 two particles (inside the white oval; Particle 3, hollow cylinders, $w_r = 0.053$ m/s), are seen deeper into the water column, and they are even momentarily moving offshore due to the breaking-induced undertow. The images presented here for Particles 1 and 3 are typical of the recorded videos. Examples of this can be seen in Videos 1 and 2 at the link provided in the Data Availability section.

Particles lying on the free surface are not necessarily captured every time a breaking wave passes. Whether or not a particle is captured depends on the location relative to the initial break point. Further into the surf zone it also depends on the slope of the breaking wave front. Generally, the video recordings show that particles located just onshore of the break point were most often captured by the breaking waves, whereas particles located either offshore or further onshore of the break point had a smaller probability of being captured. This qualitative trend is similar to that described by Deike et al. (2017), Lenain et al. (2019) and Pizzo (2017). Furthermore, the video recordings show that in the surf zone, where the waves are already breaking, it was primarily the breaking waves with steep fronts that were able to capture the buoyant particles.

4. Empirical model for the Lagrangian particle transport velocities

We will now attempt to formulate an empirical model capable of predicting the cross-shore development of the microplastic particle transport velocity u_p. To aid in the analysis we start by performing a dimensional analysis, followed by the development of such a model.

4.1. Dimensional analysis

We will now perform a dimensional analysis for the mean cross-shore Lagrangian particle velocity of a microplastic particle, u_p. At any point on a coastal profile u_p is expected to involve a functional relationship between the following 11 physical parameters:

$$u_p = f\left(H_{m0,\infty}, T_p, d_p, w_r, \nu, x, g, V, \text{profile}, \text{shape}\right) \tag{8}$$

where d_p is a characteristic length scale of the particles, ν is the kinematic water viscosity, $g = 9.81$ m/s is the gravitational acceleration, V is the wind speed (included for the sake of generality), 'profile' refers to the shape of the cross-shore profile, 'shape' refers to the particle shape and f indicates functional dependence. For the current setup with a constant slope, x and 'profile' may simply be replaced by local water depth h at least on the sloping section. For realistic profile shapes, replacing x and 'profile' with h is probably also a reasonable approach in many situations. Upon making these substitutions, Eq. (8) may be simplified to the following functional relationship now involving 10 parameters:

$$u_p = f\left(H_{m0,\infty}, T_p, d_p, w_r, \nu, g, h, V, \text{shape}\right) \tag{9}$$

From dimensional analysis the above 10 physical parameters can be reduced by two (as the physical parameters contain length and time) to the following:

$$\frac{u_p T_p}{H_{m0,\infty}} = f\left(\Omega_r = \frac{H_{m0,\infty}}{T_p w_r}, \quad Re = \frac{H_{m0,\infty}^2}{T_p \nu}, \quad \frac{d_p}{H_{m0,\infty}}, \quad \frac{H_{m0,\infty}}{T_p^2 g} \sim \frac{H_{m0,\infty}}{L_{p,\infty}}, \quad \frac{H_{m0,\infty}}{h}, \frac{H_{m0,\infty}}{T_p V}, \quad \text{shape}\right) \tag{10}$$

now only involving eight dimensionless quantities. Here Ω_r is the Dean number, Re is a Reynolds number and $H_{m0,\infty}/L_{p,\infty}$ is the deep-water characteristic wave steepness. The Reynolds number, Re, and wave steepness, $H_{m0,\infty}/L_{p,\infty}$, are typically used to classify the incoming wave climate and flow conditions. As seen from the definition, the Dean number relates the characteristic wave height to the vertical distance a particle will rise over a characteristic wave period. This non-

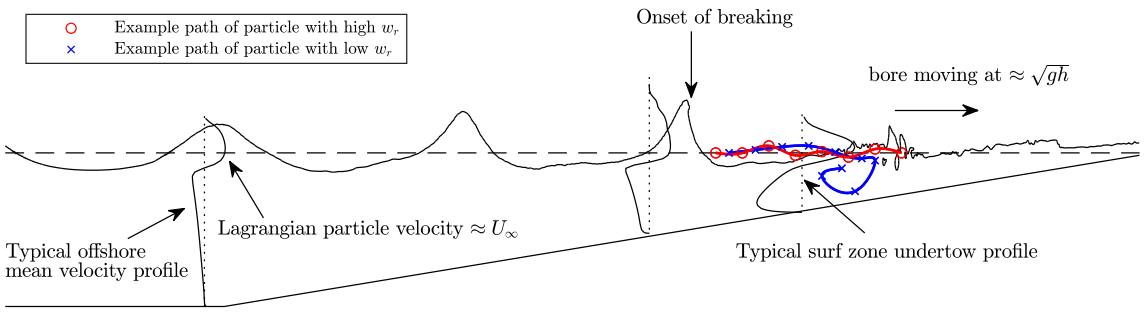

Fig. 10. Sketch of important hydrodynamic processes across the coastal profile and the typical difference in transport behavior between particles having high and low rise velocities. Surface elevations and mean velocity profiles are taken from the computational fluid dynamics simulations of Larsen and Fuhrman (2018).

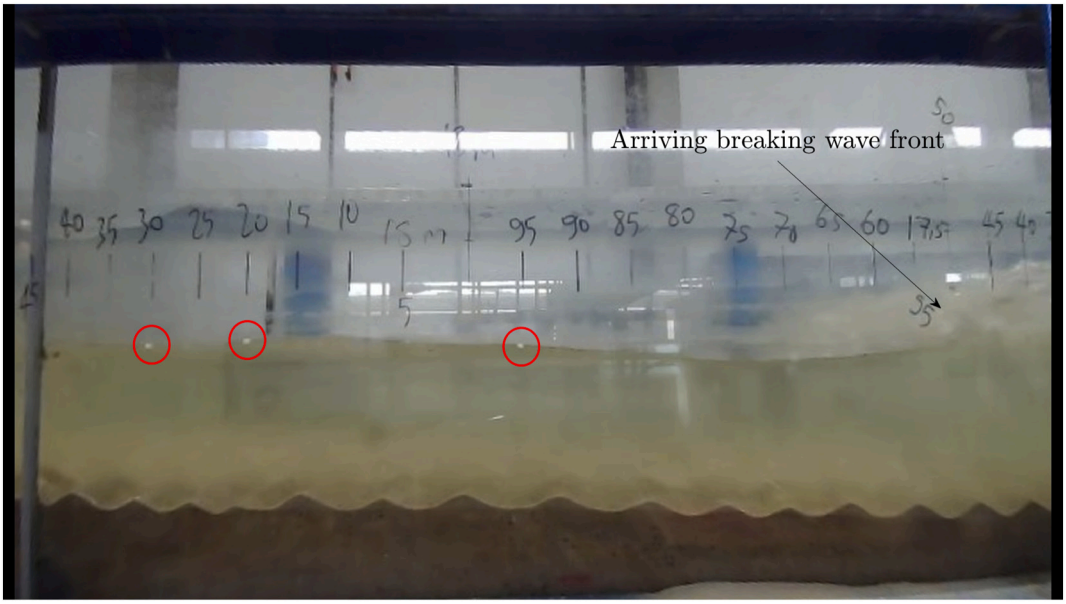

Fig. 11. Three particles (Particle 1, spheres), at $x \approx 18$ m, left by a previous breaking bore, now floating at the free-surface. The particles are inside the red circles. (For interpretation of the references to colour in this figure legend, the reader is referred to the web version of this article.)

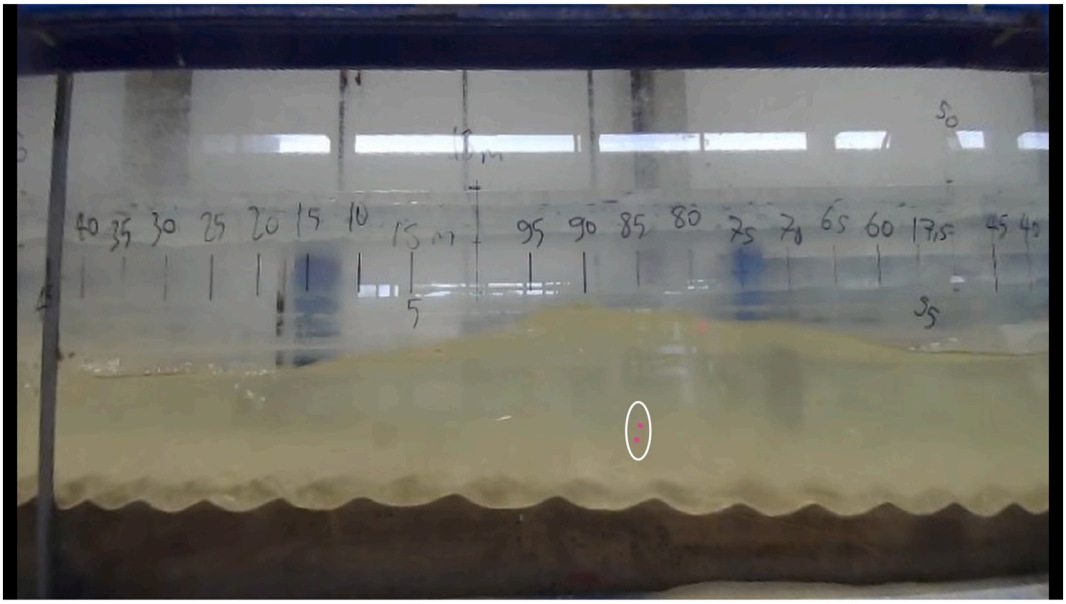

Fig. 12. Two particles (Particle 3, hollow cylinders) at $x \approx 18$ m, left behind by a previous breaking bore, now submerged deep into the water column. The particles inside the white oval have been marked with a purple marker to increase visibility. (For interpretation of the references to colour in this figure legend, the reader is referred to the web version of this article.)

dimensional number is known to be extremely important within the field of coastal sediment transport and is commonly used to predict coastal profile types (Wright and Short, 1984). Recently, Guler et al. (2022) demonstrated that accumulation hotspots of non-buoyant microplastic particles were likewise largely governed by the Dean number, thereby underlining the importance of this parameter for coastal transport of microplastic particles as well. For the Lagrangian transport velocity of buoyant microplastic particles this parameter is believed to be especially important in the surf zone, where wave breaking can cause the buoyant particles to be submerged for a significant period of time in dependence of their individual rise velocities, as discussed in Section 3.2. The wave height to local water depth ratio ($H_{m0,\infty}/h$) is likewise important, as it will largely govern the likelihood of waves breaking. Note that we utilize deep-water quantities above as proxies to avoid the complexity of having to predict or model the variation of the wave height within the surf zone. This will be discussed further in Section 5.

4.2. Empirical predictive model

We will now develop an empirical model capable of predicting the cross-shore development of u_p. The model will be inspired by the results and physical discussion and be consistent with the dimensional analysis performed above, leading to Eq. (10). In the present experiments both Reynolds number, Re, and relative particle size, d_p/H_∞, have been kept constant throughout the experiments and we had no wind. These quantities might be important, see also forthcoming discussion on the

effect of the wind in Section 5, but their dependence cannot be quantified from the present experiments and they will therefore be dropped. Furthermore, we have only tested three particle shapes (which we believe is of minor importance relative to Ω_r), and therefore we will look for an expression involving the following variables:

$$\frac{u_p T_p}{H_{m0,\infty}} = f\left(\Omega_r, \frac{H_{m0,\infty}}{L_{p,\infty}}, \frac{H_{m0,\infty}}{h}\right), \tag{11}$$

now involving only four dimensionless quantities. The next step in the development is based on three observations: (1) particles travel with a velocity close to U_∞ prior to breaking, (2) particles travel with a velocity closer to $\sqrt{gh}$ in the surf zone and (3) particles with lower Ω_r (larger w_r) tend to travel faster in the surf zone than particles with larger Ω_r (lower w_r). If we couple these three observations with the recognition that the non-dimensionalized U_∞ and $\sqrt{gh}$ can be written in terms of the non-dimensional quantities in the following way

$$\frac{U_\infty T_p}{H_{m0,\infty}} = \pi^2 \frac{H_{m0,\infty}}{L_{p,\infty}} \tag{12}$$

and

$$\frac{\sqrt{gh} T_p}{H_{m0,\infty}} = \sqrt{\frac{2\pi L_{p,\infty} h}{H_{m0,\infty}^2}}, \tag{13}$$

we propose an expression of the following form:

$$\frac{u_p T_p}{H_{m0,\infty}} = (1-Q)\frac{U_\infty T_p}{H_{m0,\infty}} + Q\frac{\sqrt{gh} T_p}{H_{m0,\infty}} \cdot min\left(\frac{Q^n}{\Omega_r}, 1\right), \tag{14}$$

where Q has an, as yet unknown, dependence on $H_{m0,\infty}/h$. The first term on the right-hand side represents the deep water wave-induced Lagrangian fluid particle velocity, which is scaled with (1-Q) to take into account the fraction of waves not breaking. The second term on the right hand side is proportional to the linear shallow water celerity, which is scaled with Q, thus accounting for the expected mean velocity of a particle when captured by surface rollers. The inverse of Ω_r in the first argument of the min function is added to reflect that particles with low Dean numbers travel faster in the surf zone, and the additional Q dependency (to some yet unknown power n) is added to reflect that particles are not always captured by the breaking waves (even in cases with very low Ω_r). Finally, the second argument of unity in the min function is included to ensure that particles are never predicted to travel faster than $Q\sqrt{gh}$.

To finalize the expression we require a method of approximating Q, and to determine the power n. For the former we suggest the following simple approximation:

$$Q = exp\left[-\left(\frac{h}{H_{m0,\infty}}\right)^2\right]. \tag{15}$$

This is inspired by Baldock et al. (1998), who in his Battjes and Janssen (1978)-type wave model, estimated Q as

$$Q = exp\left[-\left(\frac{H_b}{H_{rms}}\right)^2\right]. \tag{16}$$

Here H_b is the maximum allowed wave height at a certain water depth (using a Battjes and Janssen (1978)-type breaking criteria) and H_{rms} is the local root-mean-square wave height. The expression from Baldock et al. (1998) cannot be used without solving a differential equation for the wave energy flux, however, and therefore cannot be utilized directly in an explicit empirical model, as sought here. Therefore, we have chosen to estimate Q by Eq. (15). To test the validity of this approximation, Fig. 6e compares the measured Q from the present experiments with Eq. (15). Additionally in Fig. 13, Q from the experimental series A of Boers (2005) (having $H_{m0,\infty} = 0.17$ m) is also compared with Eq. (15). Figs. 6e and 13 show that Eq. (15) predicts the fraction of waves breaking reasonably, both in the present constant slope experiments (Fig. 6e), as well as in the more complicated barred experiments from Boers (2005) (Fig. 13). With this approximation for Q we have fitted the model to our experiments and obtained best match with $n = 0.4$. After invoking this, Eq. (14) can equivalently be written in the following simple dimensional form:

$$u_p = (1-Q)U_\infty + Q\sqrt{gh} \cdot min\left(\frac{Q^{0.4}}{\Omega_r}, 1\right). \tag{17}$$

Fig. 14 show the cross-shore development of u_p for the three particle groups, along with those predicted by Eq. (17). It can be seen that the expression captures well the increase in u_p as more waves break, and also the large differences in u_p at $x = 16$ m, which again occur due to differences in Ω_r. At $x = 14$ m it can be seen that Particle 2 (hollow cubes, $\Omega_r = 0.80$) travelled slightly faster than Particle 1 (spheres, $\Omega_r = 0.41$). This is naturally not captured by Eq. (17). A possible explanation for this discrepancy is that, by chance, a slightly higher fraction of waves broke in the case of Particle 2 compared to Particle 1. While we have demonstrated that the beaching times had converged, the fraction of waves breaking in this part of the flume is low ($Q \approx 0.05$), and therefore it would take only a few additional breaking waves in the case of Particle 2 to increase particle velocities compared to Particle 1. That the slightly higher velocity for Particle 2 is indeed by chance is further supported by Table 2, which shows that the beaching times for Particle 1 are lower than Particle 2 in all drop positions, indicating a generally faster Lagrangian particle transport velocity. At $x > 16$ m the predicted Lagrangian transport velocity first increase and then decrease towards shoreline for all three particles. The increasing trend can be explained by an increase in the fraction of breaking waves in shallower water, and the decreasing trend is caused by a decrease in the linear shallow water celerity a lower water depth.

Finally, Fig. 15 shows measured vs. predicted u_p for both the present experiments, the non-breaking experiments of Alsina et al. (2020) and the field measurements of Bjørnestad et al. (2021). In the field measurements of Bjørnestad et al. (2021), an orange rather than microplastics, was used. The orange is, of course, larger than microplastic particles, but as the oranges are buoyant and still small in size relative to the waves, the dimensional analysis, and therefore also Eq. (17), should still hold reasonably. Details of our data treatment of the field measurements from Bjørnestad et al. (2021) can be found in Appendix A. Fig. 15 demonstrates that Eq. (17) predicts the Lagrangian transport particle velocities from the present experiments well, in addition to those measured from the two prior studies.

5. Discussion

It has been shown that Eq. (17) can predict the Lagrangian transport velocities of buoyant microplastic (and other) particles well in nearshore environments, beneath both non-breaking and breaking irregular waves. It can be utilized with knowledge of particle characteristic, the incoming wave field and bathymetry. Because it is based on deep-water wave quantities, it does not require detailed modelling of the waves, and can therefore be used as a rapid and easily-applicable method to predict cross-shore Lagrangian transport velocities of buoyant microplastic (and likely other) particles. In the development of Eq. (17) we substituted 'profile' and x with h. This caused the linear shallow water celerity to show up naturally from the dimensional analysis, and allows for direct usage of $h/H_{m0,\infty}$ to predict the fraction of waves breaking in Eq. (15). For the barred profile case of Boers (2005) this expression still works well, but in situations with a wide terrace, where wave breaking can be expected to cease, Eq. (17) will likely overestimate the Lagrangian velocities due to an over-estimation of Q. To properly predict the Lagrangian velocities in such situations would require modelling the

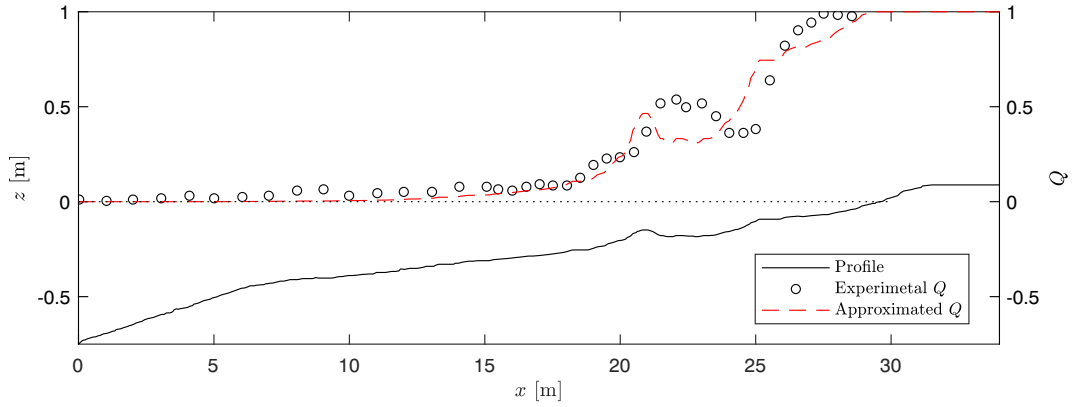

Fig. 13. Comparison of measured and approximated (using Eq. 15) fraction of waves breaking Q from (a) from present experiments and (b) those from series A of Boers (2005).

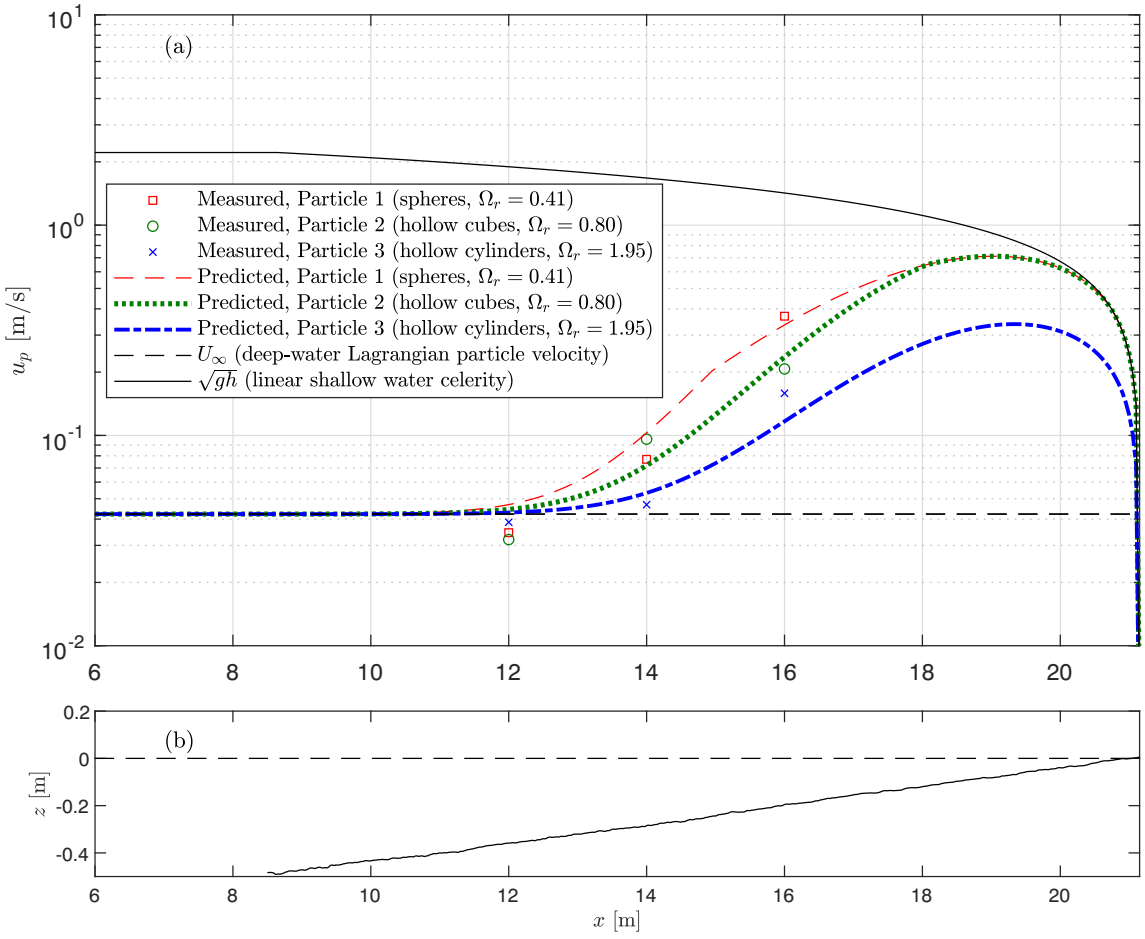

Fig. 14. (a) Comparison of measured and predicted (using Eq. 17) cross-shore Lagrangian microplastic particle transport velocities u_p and (b) bottom bathymetry.

fraction of waves breaking e.g. using a wave model like that of Battjes and Janssen (1978), coupled with the model by Southgate and Wallace (1994) for Q. If local wave heights are available from such a model or elsewhere, U_∞ in eq. (17) can be substituted with the local wave-induced Lagrangian fluid particle velocity, which can e.g. be predicted using second-order wave theory at the still water level:

$$U = \frac{H_{m0}^2 \omega_p k_p cosh(2k_p h)}{8 sinh^2(k_p h)} - \frac{H_{m0}^2 \omega_p}{8h} coth(k_p h). \quad (18)$$

The second term on the right hand side stems from the return current (compensating for the onshore volume flux near the surface), which may or may not be present in the field. Alternatively, even more advanced models like computational fluid dynamics models could be utilized.

The present experiments were performed without wind. Forsberg et al. (2020) demonstrated that an offshore-directed wind could even cause buoyant particles to be transported offshore. In their experiments the wind was extremely strong, however. In their model scale experiments the wind speed was $V = 6$ m/s. Utilizing standard Froude scaling and assuming a scaling factor of $\lambda = 50$ (corresponding to an offshore

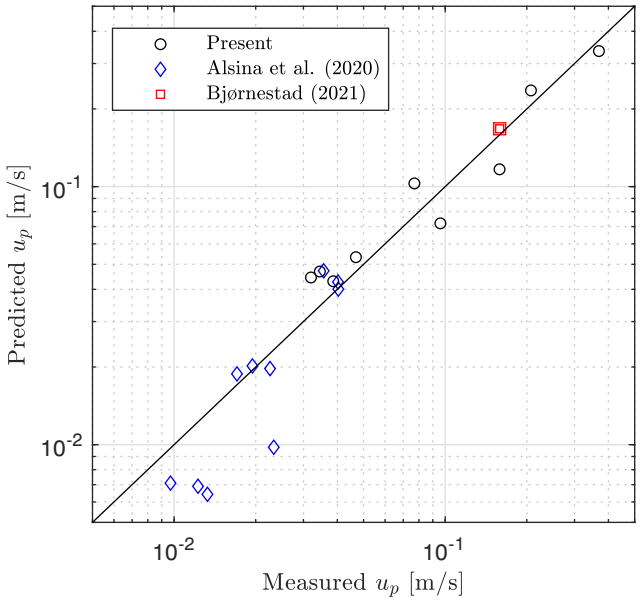

Fig. 15. Measured vs. predicted (using Eq. 17) mean Lagrangian transport velocities. The present experiments consider microplastics with $Q \approx 0$–0.2, the experiments from Alsina et al. (2020) utilized microplastic particles with $Q = 0$ and Bjørnestad (2021) consider an orange with $Q \approx 0.05$.

depth of approximately 10 m), this would correspond to a full-scale wind speed (after multiplication by $\sqrt{\lambda} \approx 7.07$) of $V = (6\text{m/s})\sqrt{\lambda} = 42$ m/s. This would thus correspond to a level one hurricane. How the Lagrangian velocities of microplastic particles will react to more moderate wind speeds remains an open question. In the deep-ocean the wind is known to create surface currents of the same order of magnitude as the Stokes drift Weber (1983) and in the pre-breaking region the wind can therefore certainly have a large effect on the Lagrangian particle transport velocities. In the surf zone the wind-induced currents may be small relative to the shallow water celerity, which we have shown governs the Lagrangian particle transport velocities in this region. The wind can, however, affect the entire wave breaking process, causing waves to break earlier (later) when they follow (oppose) the wind Douglass (1990), indicating a potential large effect of the wind in the surf zone as well.

The present experiments were performed in a pure cross-shore setting (narrow wave flume), and all particles were beached. In the field experiments of Bjørnestad et al. (2021) many oranges were released, though only the results for a single orange were presented. These oranges generally did not beach, but rather followed longshore circulation currents near the shoreline (personal communication with Prof. Henrik Kalisch). Such behavior has likewise been observed in field studies using large buoyant drifters (see e.g. MacMahan et al., 2010). Buoyant microplastic particles can be expected to behave similarly. Therefore, Eq. (17) can be expected to perform best in situations with incoming waves nearly perpendicular to the shoreline. The present model does not account for additional effects associated with longshore currents or other 3D effects such as rip currents.

Finally, the increased transport velocities of the particles due to depth-induced (nearshore) wave breaking is similar to the findings on transport velocities beneath deep-water breaking waves (Deike et al., 2017; Pizzo, 2017; Lenain et al., 2019). The present expression only accounts for depth-induced wave breaking, however. Therefore, it will not be able to predict the increased particle transport velocities due to wave breaking in deep-water. Further extension would require a means of predicting Q in deep water. This is beyond the scope of the present study, which focuses on the nearshore environment.

6. Conclusion

This work has presented new experimental measurements of the cross-shore transport and beaching times of buoyant microplastic particles in irregular (non-breaking and breaking) waves in the absence of wind. The experiments have shown that all particles were transported in the onshore direction, eventually becoming beached. Based on mean beaching times for particles released at different cross-shore positions, Lagrangian particle transport velocities have been estimated. It has been demonstrated that particles travel with velocity close to the wave-induced Lagrangian fluid particle velocity prior to breaking, in agreement with previous studies. Herein, this has been approximated simply as the deep-water value U_∞, for simplicity. In the surf zone it has been shown that the Lagrangian transport velocities of microplastic particles increase significantly, becoming closer to the wave celerity. It has been further shown that buoyant particles having low Dean number (large rise velocity) travel faster beneath breaking waves than those having high Dean number (low rise velocity). From video analysis, the reason for the Dean number dependence is that particles with larger rise velocity return to the free-surface more quickly after being submerged and left behind by a breaking wave. The video analysis has also revealed that particles with larger Dean number (lower rise velocity) can even momentarily travel offshore with the undertow, after being submerged by a breaking wave.

Using dimensional analysis, coupled with physical insight from the experiments, an empirical relation for the prediction of the cross-shore Lagrangian transport velocity of buoyant microplastic particles u_p has been developed. This is presented as Eq. (17) in the main text. This expression is demonstrated to match the present experiments well, in addition to those from two prior studies. The expression is valid for both non-breaking and (depth-induced) breaking regions, and can be utilized with knowledge of particle characteristics, the incoming wave field and the bottom bathymetry.

CRediT authorship contribution statement

Bjarke Eltard Larsen: Conceptualization, Methodology, Formal analysis, Investigation, Writing – original draft, Writing – review & editing, Visualization, Supervision, Funding acquisition. **Mustafa Ali Abdullah Al-Obaidi:** Methodology, Investigation, Formal analysis, Writing – review & editing. **Hasan Gokhan Guler:** Conceptualization, Methodology, Investigation, Writing – review & editing, Supervision, Funding acquisition. **Stefan Carstensen:** Conceptualization, Resources, Supervision, Writing – review & editing, Funding acquisition. **Koray Deniz Goral:** Methodology, Investigation, Resources, Writing – review & editing. **Erik Damgaard Christensen:** Conceptualization, Supervision, Writing – review & editing, Funding acquisition. **Nils B. Kerpen:** Conceptualization, Writing – review & editing, Funding acquisition. **Torsten Schlurmann:** Conceptualization, Writing – review & editing, Funding acquisition. **David R. Fuhrman:** Conceptualization, Methodology, Supervision, Writing – review & editing, Project administration, Funding acquisition.

Declaration of competing interest

The authors declare that they have no known competing financial interests or personal relationships that could have appeared to influence the work reported in this paper.

Data availability

The experimental data set collected in the present study is freely available at https://doi.org/10.11583/DTU.21357291. The data set provided includes the particle particle beaching times and two videos demonstrating the particle transport in the surf zone.

Acknowledgments

This research has been financially supported by the Independent Research Fund Denmark project MPCOAST: MicroPlastic transport processes in the COASTal environment, grant no. 0136-00227B. The third author additionally acknowledges financial support from The Scientific and Technical Research Council of Turkey (TUBITAK) under the 2219 International Postdoctoral Research Fellowship Programme. The authors likewise acknowledge Dr. Jose Alsina and Prof. Henrik Kalisch for discussion of their studies, enabling the comparison made in Fig. 15.

Appendix A. Lagrangian transport velocity and rise velocity of the orange from Bjørnestad et al. (2021)

The Lagrangian transport velocity of the orange has been estimated based on Fig. 3.14 of Bjørnestad (2021), which shows the path of a single orange for a duration of 74 s. During this time the orange travelled onshore over a mildly sloping bed. For the prediction of u_p for the orange a constant depth of $h = 1.9$ m has been assumed. As only one orange has been tracked the result is, of course, very dependent on the local waves encountered, and the point therefore has large uncertainty. As the orange travelled over a relatively long duration at nearly constant depth, and experienced both breaking and non-breaking waves (based on Fig. 3.14 of Bjørnestad (2021) at least one wave was breaking, as the orange disappeared, and then re-appeared 3 m further onshore after 3 s), we have opted to include it in the comparison, despite this uncertainty.

The field measurements of Bjørnestad et al. (2021) contain no information about size, density or rise velocity of the orange. Therefore, for the Ω_r estimation, the rise velocity of orange has been estimated as follows: According to Sharifi et al. (2007), the mean mass of a large orange is $m = 268.28$ g, with volume $\forall = 277.53$ cm^3, from which the diameter is estimated to be $d = 0.081$ m (assuming a spherical shape). Based on these, the typical density of an orange would be $\rho_p = 966.67$ kg/m^3. Oranges can be taken as nearly spherical, and hence their rise velocity estimated as

$$w_r = \left[\frac{-2g\left(\frac{\rho_p}{\rho} - 1\right)\forall}{C_D A}\right]^{0.5} = 0.37\,\mathrm{m/s} \tag{A.1}$$

where $A = \pi d^2/4$ is the projected cross sectional area, $\rho = 1025$ kg/m^3 the assumed seawater density and C_D is the drag coefficient, which has been determined based on the empirical expression for spheres of Schiller and Naumann (1935)

$$C_D = max\left(\frac{24}{Re_p}\left(1 + 0.15Re_p^{0.687}\right), 0.44\right). \tag{A.2}$$

This yields $C_D = 0.44$, $Re_p = dw_r/\nu = 3.0 \times 10^4$ and $w_r = 0.37$ m/s.

References

Alsina, J.M., Jongedijk, C.E., van Sebille, E., 2020. Laboratory measurements of the wave-induced motion of plastic particles: influence of wave period, plastic size and plastic density. J. Geophys. Res. Oceans 125, e2020JC016294.
Baldock, T.E., Holmes, P., Bunker, S., Van Weert, P., 1998. Cross-shore hydrodynamics within an unsaturated surf zone. Coast. Eng. 34, 173–196.
Barnes, D., Galgani, F., Thompson, R., Barlaz, M., 2009. Accumulation and fragmentation of plastic debris in global environments. Phil. Trans. Royal Soc. B 364, 1985–1998.
Battjes, J.A., Janssen, J.P.F.M., 1978. Energy loss and set-up due to breaking of random waves. In: Proc. 16th Int. Conf. Coast. Eng. Hamborg, Germany, pp. 928–941.
Bjørnestad, M., 2021. A Study of the Influence of Vorticity, Capillarity and Slope Angle on the Properties of Shoaling and Breaking Waves. University of Bergen, Bergen, Norway. Ph.D. Thesis.
Bjørnestad, M., Buckley, M., Kalisch, H., Streßer, M., Horstmann, J., Frøysa, H.G., Ige, O. E., Cysewski, M., Carrasco-Alvarez, R., 2021. Lagrangian measurements of orbital velocities in the surf zone. Geophys. Res. Lett. 48, e2021GL095722.
Boers, M., 2005. Surf Zone Turbulence. Delft Technical University, Delft, Netherlands. Ph.D. Thesis.
Brinkkemper, J.A., Lanckriet, T., Grasso, F., Puleo, J.A., Ruessink, B.G., 2016. Observations of turbulence within the surf and swash zone of a field-scale sandy laboratory beach. Coast. Eng. 113, 62–72.
Browne, M., Crump, P., Niven, S., Teuten, E., Tonkin, A., Galloway, T., Thompson, R., 2011. Accumulation of microplastic on shorelines worldwide: sources and sinks. Environ. Sci. Technol. 45, 9175–9179.
Calvert, R., McAllister, M.L., Whittaker, C., Raby, A., Borthwick, A.G., Van Den Bremer, T.S., 2021. A mechanism for the increased wave-induced drift of floating marine litter. J. Fluid Mech. 915, A73.
Cozar, A., Echevarria, F., Gonzalez-Gordillo, I., Irigoien, X., Ubeda, B., Hernandez-Leon, S., Palma, A., Navarro, S., de Lomas, J.G., Ruiz, A., de Puelles, M.F., Duarte, C., 2014. Plastic debris in the open ocean. Proc. Natl. Acad. Sci. U. S. A. 111, 10239–10244.
Deike, L., Pizzo, N., Melville, W.K., 2017. Lagrangian transport by breaking surface waves. J. Fluid Mech. 829, 364–391.
Douglass, S.L., 1990. Influence of wind on breaking waves. J. Waterw. Port C-ASCE 116 (6), 651–663.
Forsberg, P.L., Sous, D., Stocchino, A., Chemin, R., 2020. Behaviour of plastic litter in nearshore waters: first insights from wind and wave laboratory experiments. Mar. Pollut. Bull. 153, 111023.
Galvin, C.J., 1968. Breaker type classification on three laboratory beaches. J. Geophys. Res. 73, 3651–3659.
Guler, H.G., Larsen, B.E., Quintana, O., Goral, K.D., Carstensen, S., Christensen, E.D., Kerpen, N.B., Schlurmann, T., Fuhrman, D.R., 2022. Experimental study of non-buoyant microplastic transport beneath breaking irregular waves on a live sediment bed. Mar. Pollut. Bull. 181, 113902.
Jambeck, J.R., Geyer, R., Wilcox, C., Siegler, T.R., Perryman, M., Andrady, A., Narayan, R., Law, K.L., 2015. Plastic waste inputs from land into the ocean. Science 347, 768–771.
Kerpen, N.B., Schlurmann, T., Schendel, A., Gundlach, J., Marquard, D., Hüpgen, M., 2020. Wave-induced distribution of microplastic in the surf zone. Front. Mar. Sci. 7 (590565).
Kooi, M., Nes, E.H.V., Scheffer, M., Koelmans, A.A., 2017. Ups and downs in the ocean: effects of biofouling on vertical transport of microplastics. Environ. Sci. Technol. 51, 7963–7971.
Lamb, J., Willis, B., Fiorenza, E., Couch, C., Howard, R., Rader, D., True, J., Kelly, L., Ahmad, A., Jompa, J., Harvell, C., 2018. Plastic waste associated with disease on coral reefs. Science 359, 460–462.
Larsen, B.E., Fuhrman, D.R., 2018. On the over-production of turbulence beneath surface waves in Reynolds-averaged navier-stokes models. J. Fluid Mech. 853, 419–460.
Larsen, B.E., van der A, D.A., van der Zanden, J., Ruessink, G., Fuhrman, D.R., 2020. Stabilized RANS simulation of surf zone kinematics and boundary layer processes beneath large-scale plunging waves over a breaker bar. Ocean Model. 155, 101705.
Larsen, B.E., van der A, D.A., Carstensen, R., Carstensen, S., Fuhrman, D.R., 2023. Experimental investigation on the effect of placement and timing of shoreface nourishments. Coast. Eng. 180, 104258.
Lenain, L., Pizzo, N., Melville, W.K., 2019. Laboratory studies of lagrangian transport by breaking surface waves. J. Fluid Mech. 876, R1.
MacMahan, J., Brown, J., Brown, J., Thornton, E., Reniers, A., Stanton, T., Henriquez, M., Gallagher, E., Morrison, J., Austin, M.J., Scott, T.M., Senechal, N., 2010. Mean lagrangian flow behavior on an open coast rip-channeled beach: a new perspective. Mar. Geol. 268, 1–15.
Nerland, I., Halsband, C., Allan, I., Thomas, K., 2014. Microplastics in Marine Environments: Occurrence, Distribution and Effects. Tech. Rep. 6754-2014. Norwegian Institute for Water Research, Oslo.
Pizzo, N.E., 2017. Surfing surface gravity waves. J. Fluid Mech. 823, 316–328.
Schiller, L., Naumann, Z., 1935. A drag coefficient correlation. Zeit. Ver. Deutsch. Ing. 77, 318–320.
van Sebille, E., Wilcox, C., Lebreton, L., Maximenko, N., Hardesty, B., van Franeker, J., Eriksen, M., Siegel, D., Galgani, F., Law, K., 2015. A global inventory of small floating plastic debris. Environ. Res. Lett. 10, 124006.

van Sebille, E., Aliani, S., Law, K.L., Maximenko, N., Alsina, J.M., Bagaev, A., Bergmann, M., Chapron, B., Chubarenko, I., Cózar, A., Delandmeter, P., Egger, M., Fox-Kemper, B., Garaba, S.P., Goddijn-Murphy, L., Hardesty, B.D., Hoffman, M.J., Isobe, A., Jongedijk, C.E., Kaandorp, M.L.A., Wichmann, D., 2020. The physical oceanography of the transport of floating marine debris. Environ. Res. Lett. 15, 023003.

Sharifi, M., Rafiee, S., Keyhani, A., Jafari, A., Mobli, H., Rajabipour, A., Akram, A., 2007. Some physical properties of orange (var. tompson). Int. Agrophys. 21, 391–397.

Southgate, H.N., Wallace, H.M., 1994. Breaking wave persistence in parametric surf zone models. In: Coastal Dynamics '94, pp. 543–555.

Sumer, B.M., Fuhrman, D.R., 2020. Turbulence in Coastal and Civil Engineering. World Scientific.

Weber, J.E., 1983. Steady wind-induced and wave-induced currents in the open ocean. J. Phys. Oceanogr. 13, 524–530.

Wieczorek, A., Morrison, L., Croot, P., Allcock, A., MacLoughlin, E., Savard, O., Brownlow, H., Doyle, T., 2018. Frequency of microplastics in mesopelagic fishes from the Northwest Atlantic. Front. Mar. Sci. 5.

Wright, L., Short, A., 1984. Morphodynamic variability of surf zones and beaches - a synthesis. Mar. Geol. 56, 93–118.

Zhang, H., 2017. Transport of microplastics in coastal seas. Estuar. Coast. Shelf Sci. 199, 74–86.